Research Square

Preprints are preliminary reports that have not undergone peer review.
They should not be considered conclusive, used to inform clinical practice,
or referenced by the media as validated information.

Numerical Comparison of Pressure Drop in 90° Bend Layouts in Dilute-Phase Pneumatic Conveying

Lemi Demissie Boset

lemid@du.edu.et

Dilla University

Research Article

Keywords: 90° bend layout, CFD-DPM, dilute-phase pneumatic conveying, pipe diameter, pressure drop, RNG k-ε turbulence model

Posted Date: November 6th, 2026

DOI: https://doi.org/10.21203/rs.3.rs-10780978/v1

License: This work is licensed under a Creative Commons Attribution 4.0 International License.
Read Full License

Additional Declarations: No competing interests reported.

Numerical Comparison of Pressure Drop in 90° Bend Layouts in Dilute-Phase Pneumatic Conveying

Lemi Demissie Boset

Department of Mechanical Engineering, College of Engineering, Dilla University, Dilla, Ethiopia

Corresponding author email: lemid@du.edu.et

Abstract

Bend configuration influences pressure loss in dilute-phase pneumatic conveying by altering flow direction, particle momentum, and particle-wall interactions. This study compared five 90° bend layouts (horizontal-to-horizontal, H-H; horizontal-to-vertical down, H-V DOWN; vertical-to-horizontal left, V-H LEFT; vertical-to-horizontal right, V-H RIGHT; and horizontal-to-vertical up, H-V UP) using two-way coupled Euler-Lagrange CFD-DPM simulations with the RNG k-ε turbulence model. Every layout was simulated at the same 144 operating conditions, drawn from a grid of three pipe diameters (0.046, 0.071 and 0.120 m), six inlet air velocities (12-28 m/s) and twelve solids mass-flow rates (0.009-0.28 kg/s), giving 720 simulations; combinations at high solids loading and low velocity were not simulated. Pressure drop was evaluated between planes 1D upstream and 10D downstream of the bend. Against published experimental data, the model reproduced single-phase and gas-solid pressure drops with mean absolute relative errors of 3.40% and 4.65% (maximum 5.21%) for the tabulated cases. The overall mean pressure drop was highest for V-H LEFT (185.07 Pa) and lowest for H-V UP (141.31 Pa), a difference of 43.76 Pa (23.7%). Because the layouts share the same conditions, they were compared with a randomised-block ANOVA with operating condition as the block: the layout effect was highly consistent ($F(4, 572) = 291.0$, $p < 0.001$), all ten pairwise differences were significant after Holm adjustment, and the ranking V-H LEFT > H-V DOWN > H-H > V-H RIGHT > H-V UP held in 143 of the 144 conditions (one tie). Pipe diameter, air velocity and solids mass-flow rate controlled the magnitude of the pressure drop, while the layout acted as a nearly constant multiplier (about 0.90 to 1.22 times the H-H value), with layout × condition interactions that were detectable but small. Bend orientation is therefore a practical design variable, but the results are simulation-based and the layout mechanisms remain to be confirmed experimentally.

Keywords: 90° bend layout; CFD-DPM; dilute-phase pneumatic conveying; pipe diameter; pressure drop; RNG k-ε turbulence model

1. Introduction

In dilute-phase pneumatic conveying systems, solid particulate matter is transported through continuous piping networks using high-velocity gas carriers [1]. Boset demonstrated that numerical CFD-DPM simulations integrated with artificial neural networks effectively map pressure drop in positive dilute-phase teff grain transport [1]. While uniform frictional head loss occurs along straight pipe lengths, geometrical discontinuities most notably 90° bends introduce severe flow disturbances, local particle deceleration, momentum dissipation, and aggressive wall impacts [2]. Kuang et al. showed via CFD-DEM simulations that gas-solid flow patterns in pneumatic conveying pipelines are heavily disrupted by bend curvature [2]. These complex phenomena make bends the primary contributors to localized pressure drop, elevated power consumption, and mechanical wear throughout industrial piping systems [3]. Senapati and Dash emphasized that multiphase CFD-DPM modeling provides critical insights into particle dynamic

behaviors within complex bend geometries [3]. Developing an accurate predictive understanding of pressure loss across diverse bend configurations remains a vital mandate in fluid power engineering and bulk solids handling [4]. Inaba and Husain conducted experimental and numerical evaluations establishing the two-phase flow pressure drop characteristics in piping systems [4].

When a gas-solid two-phase mixture navigates a 90° elbow, centrifugal acceleration forces dense solid particles toward the outer wall, generating localized secondary flow structures and concentrated particle ropes [5]. Dutta established that RNG k-epsilon turbulence closures accurately model secondary flows and turbulent momentum exchange in multiphase systems [5]. This spatial redistribution induces rapid kinetic energy dissipation via intensive particle-wall impact collisions [6]. Dutta et al. analyzed particle-wall collision dynamics using CFD-DPM to highlight the main mechanisms of energy loss in bends [6]. Pressure losses are further governed by variations in fluid-particle drag forces [7]. Moujaes and Deshmukh provided detailed characteristics of pressure loss mechanisms occurring specifically across 90° pipe bends in dilute-phase transport [7]. Inter-particle friction and particle concentration gradients also drive local pressure differentials [8]. Klinzing et al. documented fundamental design equations and operating principles for industrial bulk solids handling in pneumatic conveying pipelines [8].

Upon exiting the bend curvature, the decelerated particles must be re-accelerated to their terminal conveying velocity by the surrounding gas stream [9]. Marcus et al. detailed the underlying physics of particle acceleration zones and associated pressure penalties in pneumatic conveying lines [9]. This post-bend acceleration phase establishes a substantial downstream acceleration pressure drop alongside the primary local bend head loss [10]. Bradley formulated empirical relations describing pressure drop behavior across bends and downstream acceleration zones in pneumatic lines [10]. Because spatial orientation directly governs the coupling between gravitational forces, fluid drag, and particle inertia [11], McGlinchey highlighted that proper equipment selection and layout geometry are paramount to minimizing system resistance [11]. The spatial direction of a bend strongly dictates internal two-phase flow dynamics across layout variations [12]. Huber and Sommerfeld modeled dilute-phase pneumatic conveying in pipe systems to illustrate how layout changes affect particle distribution [12].

Spatial orientations such as horizontal-to-horizontal layouts exhibit distinct flow structures [13]. Sommerfeld and Lain investigated particle motion and deposition in turbulent pipe bends to explain gravity-driven phase separation [13]. In horizontal-to-horizontal configurations, particles remain confined to a single horizontal plane where transverse collisions and secondary flow vortices govern flow resistance [14]. Zenz and Othmer established foundational fluidization and fluid-particle principles governing horizontal two-phase flow regimes [14]. Variations extend to horizontal-to-vertical down arrangements [15]. Levy formulated two-phase flow models that capture particle distribution shifts in pneumatic conveying lines [15]. Particle roping varies significantly depending on whether the flow transitions vertically or horizontally [16]. Mason and Levy simulated particle roping phenomena in pneumatic conveying bends to demonstrate spatial variations in solids concentration [16].

In vertical-to-horizontal left configurations, flow orientation alters the angle of particle impact against pipe walls [17]. Yilmaz and Levy investigated particle attenuation and pressure drop in pneumatic elbows under varying flow directions [17]. Conversely, in horizontal-to-vertical down arrangements, gravitational acceleration assists forward

particle motion to partially counterbalance wall friction [18]. Chen and Pereira computed gas-solid two-phase flows in curved ducts, proving that gravity influences velocity profiles [18]. Vertical-to-horizontal right configurations require particles to overcome severe momentum loss entering horizontal runs [19]. Zhang and Li provided numerical predictions of pressure drop in horizontal-to-vertical pneumatic conveying bends [19]. Horizontal-to-vertical up layouts force particles to overcome both severe momentum losses and opposing gravitational potential energy gradients [20]. Wang and Shirley analyzed particle impact and wall erosion dynamics to confirm increased resistance in upward vertical transport [20].

Recent advancements in multiphase computational fluid dynamics (CFD) facilitate comprehensive numerical investigations of complex gas-solid flows using coupled Euler-Lagrange framework formulations [21]. Solnordal and Frank simulated multiphase pressure losses across industrial elbow configurations using advanced CFD methodologies [21]. The Discrete Phase Model (DPM) tracks individual particle trajectories by integrating force balance differential equations [22]. Tsuji et al. pioneered discrete particle simulations of gas-solid flows in pneumatic lines using Lagrangian tracking [22]. Force balances within the model account for gravitational forces [23]. Bilirgen and Levy evaluated the mixing and dispersion of solid particles in pipe bends under gravitational and turbulent forces [23]. DPM formulations also incorporate local pressure gradients [24]. Kuan et al. modeled dilute phase pneumatic conveying around elbows to capture pressure-gradient forces on particles [24]. Furthermore, external user-defined forces are routinely integrated into the Eulerian-Lagrangian framework [25]. Rose and Duckworth formulated early generalized relationships for the transport of solid particles in fluid streams [25].

When integrated with advanced turbulence models such as the Re-Normalization Group (RNG) k-ε formulation, numerical simulations accurately model turbulent kinetic energy and secondary flows near curved boundaries [26,27]. Chambers and Marcus demonstrated methods for designing pneumatic conveying bends to minimize pressure drop and erosion [26]. Westman and Michael conducted CFD analyses of gas-solid two-phase flow through 90 degree elbows using RNG closure models [27]. CFD-DPM effectively captures turbulent kinetic energy generation, boundary layer interaction, and localized pressure fields across intricate piping geometries [28]. Turton and Levenspiel established engineering correlations to predict the terminal velocity and drag of spherical particles in fluid media [28]. Particle drag calculations are refined using non-spherical drag models [29]. Haider and Levenspiel developed drag coefficient correlations for non-spherical particles to improve multiphase tracking accuracy [29].

2. Materials and Methods

2.1 Material

Teff grain was used as the dispersed phase. Its sphericity ranges from 0.67 to 0.70 (mean 0.68) and its particle density from 1,120 to 1,381 kg/m³ [45]. The simulations used a particle density of 1,120 kg/m³ and a mean particle diameter of 0.68 mm (minimum 0.54 mm, maximum 0.82 mm), with the size distribution represented by the Rosin-Rammler model. Because teff grains are non-spherical, a non-spherical drag law with a shape factor of 0.76 was applied.

2.2 CFD-DPM modeling in ANSYS Fluent

The Discrete Phase Model (DPM) is a Lagrangian approach within the Euler-Lagrange framework. Particle trajectories are calculated by integrating the particle force-balance equation until the continuous-phase solution converges [22]. The governing equation is:

$$\frac{du_p}{d_t} = F_d(u - u_p) + \frac{g(\rho_p - \rho)}{\rho_p} + F \tag{1}$$

where u_p and u are the particle and fluid velocities, respectively; ρ_p and ρ are the particle and fluid densities; F_d is the drag coefficient term; and F represents additional forces. The drag expression used for particle tracking is:

$$F_d = \frac{18\mu C_D \,\mathrm{Re}}{\rho_p d_p^2 24} \tag{2}$$

where Re is the particle Reynolds number, μ is the dynamic viscosity of air, and C_D is the particle drag coefficient, determined according to the selected particle-shape model.

2.3 Turbulence model

Turbulent effects must be considered when modeling the high-speed internal airflow in the conveying pipe. The Reynolds-averaged continuity and momentum equations are written as follows [22]:

$$\frac{\partial \rho}{\partial t} = \nabla.(\rho \vec{v}) = S_m \tag{3}$$

where ρ is fluid density, t is time, v is the three-dimensional velocity vector, and S_m is a source term.

$$\frac{\partial \rho}{\partial t} + \nabla\rho(\vec{v}.\vec{v}) = \nabla.p + \nabla\bar{\bar{T}} + \nabla\rho(\overline{\vec{v}'.\vec{v}'}) + \rho\vec{g} + \vec{F} \tag{4}$$

where g is gravitational acceleration, F is a source term, and T is the viscous stress tensor defined as:

$$\bar{\bar{T}} = \mu\left[(\nabla\vec{v} + \nabla v^{\vec{T}}) - \frac{2}{3}\nabla.\vec{v}I\right] \tag{5}$$

where μ is the dynamic viscosity and I is the identity tensor.

The Renormalization Group (RNG) k-ε turbulence model was selected to represent turbulent airflow through the bends. Compared with the standard k-ε model, the RNG formulation includes a modified dissipation-rate equation and analytically derived turbulent Prandtl numbers, which can improve predictions for rapidly strained and swirling flows [5, 33]. The transport equations for turbulent kinetic energy, k, and its dissipation rate, ε, are:

$$\frac{\partial \rho k}{\partial t} + \nabla\rho(k.\vec{v}) = \nabla.(\mu + \frac{\mu_T}{\sigma_k} * \nabla k) + G_k + G_k + \rho\varepsilon + Y_M + S_k \tag{6}$$

$$\frac{\partial \rho\varepsilon}{\partial t} + \nabla\rho(\varepsilon.\vec{v}) = \nabla.(\mu + \frac{\mu_T}{\sigma_\varepsilon} * \nabla\varepsilon) + C_{1\varepsilon}\frac{\varepsilon}{k} + (G_k + C_{3\varepsilon}G_b) - C_{2\varepsilon}\rho\frac{\varepsilon^2}{k} + S_\varepsilon \tag{7}$$

where Y_M accounts for compressibility effects on turbulence, G_k is the generation of turbulence due to the velocity gradients (local strain), G_b is the generation of turbulence due to buoyancy effects, and σ_k and are the turbulent Prandtl numbers for k and ε. $C_{1\varepsilon}$, $C_{2\varepsilon}$, $C_{3\varepsilon}$ and in the dissipation rate equation are constants that are derived by calibration with experiments, and S_k and S_ε are user defined source terms. The local solution for k - ε enables calculation of the local eddy viscosity, which takes the form: The eddy viscosity can be found in the momentum equations as well as the k and ε equations, indicating a strong coupling in the solution process [5, 33].

2.4 Domain geometry and simulation setup

The 3D geometric domain was constructed using ANSYS SpaceClaim 2024 R1. Five 90° bend layout orientations were investigated: horizontal-to-horizontal (H-H), horizontal-to-vertical down (H-V DOWN), vertical-to-horizontal left (V-H LEFT), vertical-to-horizontal right (V-H RIGHT), and horizontal-to-vertical up (H-V UP). Each domain consists of an upstream straight pipe of length L1 = 1.0 m, a 90° circular-arc bend with centreline radius Rb = 6D, and a downstream straight pipe of length L2 = 2.0 m, where D is the pipe diameter (0.046, 0.071 or 0.120 m). With the same absolute lengths for all three diameters, L1 equals 21.7D, 14.1D and 8.3D and L2 equals 43.5D, 28.2D and 16.7D, respectively.

Operating-condition matrix. The operating conditions were drawn from a grid of three pipe diameters (D = 0.046, 0.071 and 0.120 m), six inlet air velocities (v = 12, 16, 18, 22, 25 and 28 m/s) and twelve solids mass-flow rates ($\dot{m}_s$ = 0.009, 0.030, 0.044, 0.067, 0.084, 0.10, 0.13, 0.16, 0.19, 0.22, 0.25 and 0.28 kg/s). The full grid has 3 × 6 × 12 = 216 combinations, of which 144 were simulated (29 for D = 0.046 m, 45 for D = 0.071 m and 70 for D = 0.120 m). The simulated set is therefore not a full factorial: the highest solids mass-flow rate is 0.10 kg/s for D = 0.046 m, 0.25 kg/s for D = 0.071 m and 0.28 kg/s for D = 0.120 m, and at each diameter the lowest velocity simulated rises as the solids mass-flow rate increases (Supplementary Table S1). All five layouts were simulated at each of the 144 conditions, giving 5 × 144 = 720 simulations with one simulation per layout and condition; the complete results are listed in Supplementary Table S1.

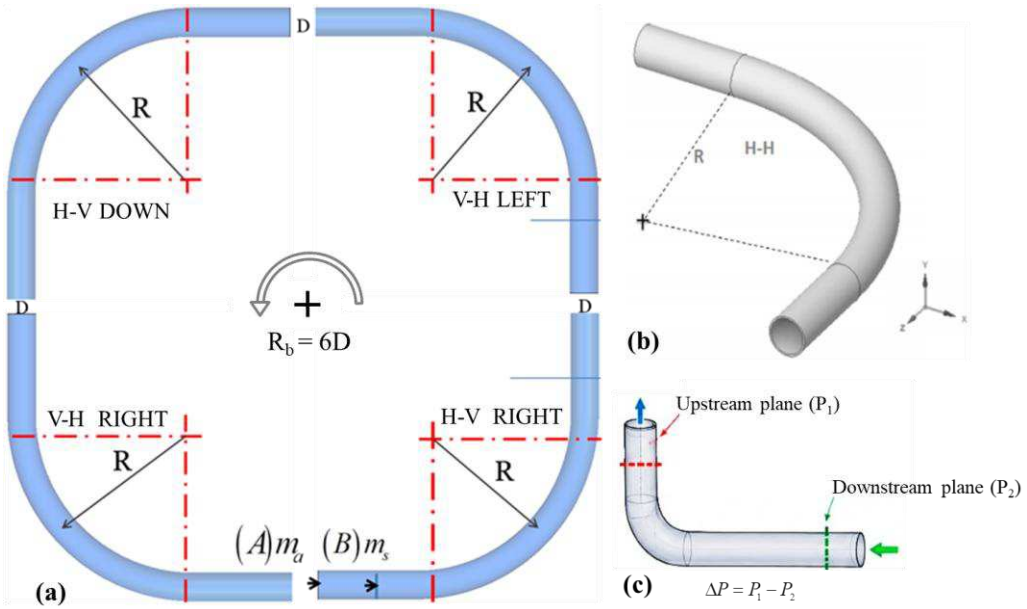


Figure 1. Computational geometries of the five 90° bend layouts: (a) H-V UP, V-H LEFT, H-V DOWN, and V-H RIGHT; (b) H-H; and (c) upstream and downstream pressure-measurement planes

Figure 1 defines the geometric differences considered in the comparison and identifies the pressure-measurement locations. Keeping the measurement planes at the same relative positions for each layout is important because it makes the calculated pressure drops more comparable across configurations.

Static pressure drop across the bend layout (ΔP) is determined from area-weighted average static pressures on specified measurement planes:

$$\Delta P = P_1 - P_2 \tag{8}$$

where P_1 is the area-weighted average static pressure on a plane 1D upstream of the bend inlet and P_2 is the area-weighted average static pressure on a plane 10D downstream of the bend outlet; both planes are perpendicular to the pipe axis (Figure 1c). ΔP is therefore the total static-pressure change over the bend and the adjoining straight lengths (1D upstream and 10D downstream), including particle re-acceleration downstream of the bend and, for layouts with a change in elevation, the gravitational pressure change between the planes. The planes are defined in the same way for all layouts and diameters.

2.5 Boundary conditions and phase coupling

Continuous-phase boundary conditions: At the pipe inlet, air is introduced with uniform axial velocity (12, 16, 18, 22, 25, 28 m/s) and standard air properties (density $\rho = 1.225$ kg/m³, dynamic viscosity $\mu = 1.7894 \times 10^{-5}$ kg/(m·s)). At the pipe outlet, a pressure-outlet condition with gauge pressure fixed at 0 Pa is prescribed. Pipe walls are modeled as smooth, stationary rigid boundaries with standard wall functions. Air enters along the z-axis.

Discrete-phase boundary conditions and coupling: Two-way phase coupling is enabled, allowing momentum and turbulence transfer between the gas and solid phases at every fluid iteration step. Teff grains are injected uniformly

across the inlet surface. At the outlet, particles escape the domain (escape boundary condition). At the pipe walls, a reflect boundary condition is applied using wall restitution coefficients [6]: normal restitution coefficient en = 0.90 and tangential restitution coefficient et = 0.85. Gravitational acceleration is set to -9.81 m/s² along the vertical Y-axis.

2.6 Solution method and convergence criteria

The pressure-based solver of ANSYS Fluent was used with SIMPLE pressure-velocity coupling. Pressure was discretised with a second-order scheme, and momentum, turbulent kinetic energy and dissipation rate with second-order upwind schemes. Each case was run for 500-1000 iterations, with the discrete phase coupled to the gas phase at every fluid iteration. Convergence required scaled residuals below 1×10^{-5} for continuity, 1×10^{-6} for velocity, 1×10^{-6} for the turbulence quantities and 1×10^{-5} for the discrete phase. In addition, the area-weighted static pressures on the two measurement planes were monitored until they stabilised.

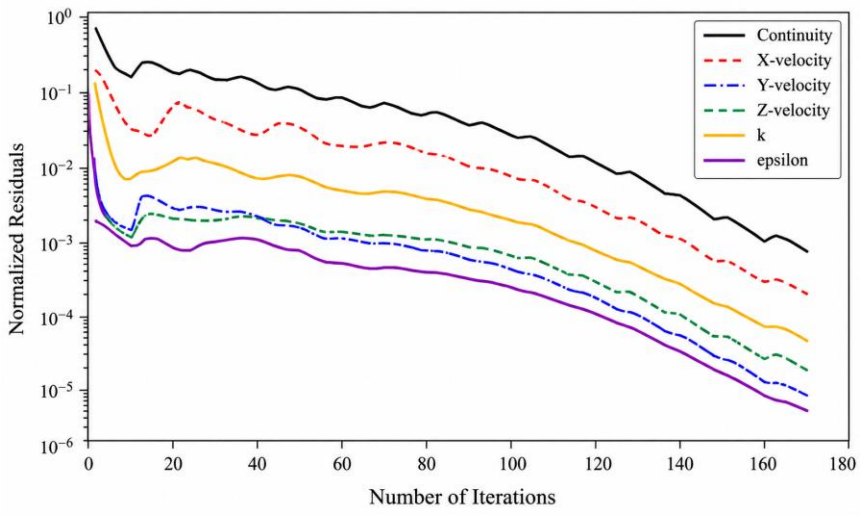


Figure 2. Scaled residuals for the 71-mm H-V UP bend at v = 20 m/s and $\dot{m}_s$ = 0.13 kg/s

Figure 2 shows the scaled residual history for the illustrated case, in which the residuals fall to the targets above and then stabilise. Residual levels, the stability of the monitored plane pressures and the global mass balance were used together as the convergence criteria for all 720 simulations.

2.7 Mesh sensitivity and grid independence

A mesh-sensitivity study was carried out for D = 0.071 m, v = 20 m/s and $\dot{m}_s$ = 0.13 kg/s. The velocity of 20 m/s lies within the tested range (12-28 m/s) and was chosen as a mid-range representative case; it is not one of the six matrix velocities. The mesh size was varied from 10.00 mm to 2.72 mm. Following the recommendation that the cell size should exceed four particle diameters in CFD-DPM [13], the finest mesh (2.72 mm) corresponds to a mesh-size-to-mean-particle-diameter ratio of 4.0 for the 0.68 mm teff grains, and the selected 4.50-mm mesh to a ratio of 6.6.

Table 1. Mesh-sensitivity and grid-independence results for D = 0.071 m, v = 20 m/s, and $\dot{m}_s$ = 0.13 kg/s

Mesh Size (mm)	Cell Count	Y^+ Range	Pressure Drop (Pa)	Relative Error vs. 2.72 mm (%)
10.00	91,347	248.5	230.1	53.3%
6.25	372,861	182.1	157.0	4.6%
4.50 (Selected)	1,003,284	132.4	153.0	1.9%
3.50	2,124,763	98.2	151.8	1.1%
2.72	4,525,192	72.1	150.1	Reference

Note. Y^+ is the dimensionless wall distance. Relative error is the difference from the finest mesh (2.72 mm) divided by its pressure drop (150.1 Pa). The 4.50-mm mesh was selected for all simulations.

Table 1 shows that the predicted pressure drop falls from 230.1 Pa on the coarsest mesh to 153.0 Pa on the selected 4.50-mm mesh, which differs from the finest-mesh result (150.1 Pa) by 2.9 Pa (1.9%). Successive changes between the three finest meshes (1.2 Pa and 1.7 Pa) are small and do not decrease monotonically, so the asymptotic range required for a Richardson-extrapolation grid convergence index is not demonstrated, and these differences are of the order expected from stochastic particle tracking. The numerical uncertainty due to discretisation is therefore reported conservatively as 1.9% (selected versus finest mesh). The Y+ values of 72-248 lie within the range of 30-300 for which standard wall functions are valid.

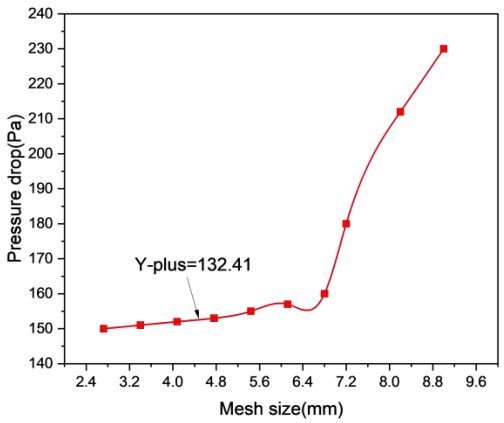


Figure 3. Predicted static pressure drop as a function of mesh size for the grid-independence assessment. The 4.50-mm mesh was selected for the simulations (y^+ = 132.41)

Figure 3 shows the pressure-drop prediction becoming insensitive to refinement below about 4.5 mm: 153.0 Pa at 4.50 mm, 151.8 Pa at 3.50 mm and 150.1 Pa at 2.72 mm. The selected mesh is a compromise between accuracy and computational cost for the 720 simulations, with the 1.9% uncertainty stated above.

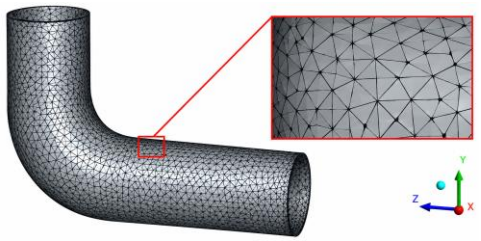


Figure 4. Computational mesh for the 71-mm V-H RIGHT bend layout

Figure 4 shows the mesh used to resolve the bend and the adjacent straight pipes. Mesh independence is established by the quantitative results in Table 1 rather than by the image.

2.8 Numerical model validation

The CFD-DPM model was checked quantitatively against published experimental pressure-drop data (Table 2). The comparison cases were simulated with the same turbulence model, phase coupling, wall treatment, solver settings and mesh-sizing criterion as the main study.

Single-phase flow: predictions were compared with experimental pressure-loss data of Moujaes and Deshmukh [7] for air flow through 90° bends (D = 0.050 m, $R_b/D = 6$) at inlet velocities of 10-30 m/s. The three cases in Table 2 give a mean absolute relative error (MARE) of 3.40%.

Gas-solid flow: two-phase pressure drops were compared with the experimental measurements of Yuan et al. [47] for 90° bends at different solids loadings. The two cases in Table 2 give a MARE of 4.65%. The Yuan et al. study concerns dense-phase conveying at high pressure; the cases used here are those at velocities and loadings representative of the present dilute-phase range, and the comparison does not validate the model for dense-phase conditions.

Table 2. Validation of CFD-DPM pressure-drop predictions against experimental benchmark data

Validation Case	Air Velocity (m/s)	Solids Loading	Exp. ΔP (Pa)	CFD-DPM ΔP (Pa)	Relative Error (%)
Moujaes & Deshmukh [7] (Single Phase)	12.0	0.0	42.5	43.8	+3.06%
Moujaes & Deshmukh [7] (Single Phase)	20.0	0.0	118.0	122.1	+3.47%
Moujaes & Deshmukh [7] (Single Phase)	28.0	0.0	231.0	239.5	+3.68%
Yuan et al. [47] (Two-Phase Dilute)	16.0	m_s = 0.03 kg/s	95.2	99.1	+4.10%
Yuan et al. [47] (Two-Phase Dilute)	25.0	m_s = 0.10 kg/s	242.0	254.6	+5.21%

Note. ΔP denotes pressure drop. Solids loading is expressed as the solids mass-flow rate ($\dot{m}_s$). MARE is the mean of the absolute relative errors of the cases listed: 3.40% (single phase, n = 3), 4.65% (gas-solid, n = 2) and 3.90% (all five cases).

The relative errors range from 3.06% to 3.68% for the single-phase cases and from 4.10% to 5.21% for the gas-solid cases, i.e., the model over-predicts the measured pressure drop in every case, with larger deviations when particles

are present. The maximum error is 5.21%. No particle-trajectory measurements were available for these datasets, so the particle-wall interaction results in Section 3.2 are qualitative, and pressure drop is the only quantity validated.

3. Results and Discussion

3.1 General pressure-drop trends across bend orientations

Across the 720 simulations (the same 144 operating conditions for each of the five layouts), predicted static pressure drop varied with bend orientation, inlet air velocity, solids mass-flow rate, and pipe diameter. The results indicate that pressure loss is controlled by the combined operating conditions rather than by bend geometry alone. Increasing air velocity generally raises pressure drop because the gas carries greater momentum and transfers more momentum to the particles and pipe wall; increasing solids loading can further increase gas-solid momentum exchange and collision-related losses [8, 46]. The diameter effect should be interpreted in the context of the tested combinations, because changing diameter also changes the flow area and the gas-solid flow structure [37].

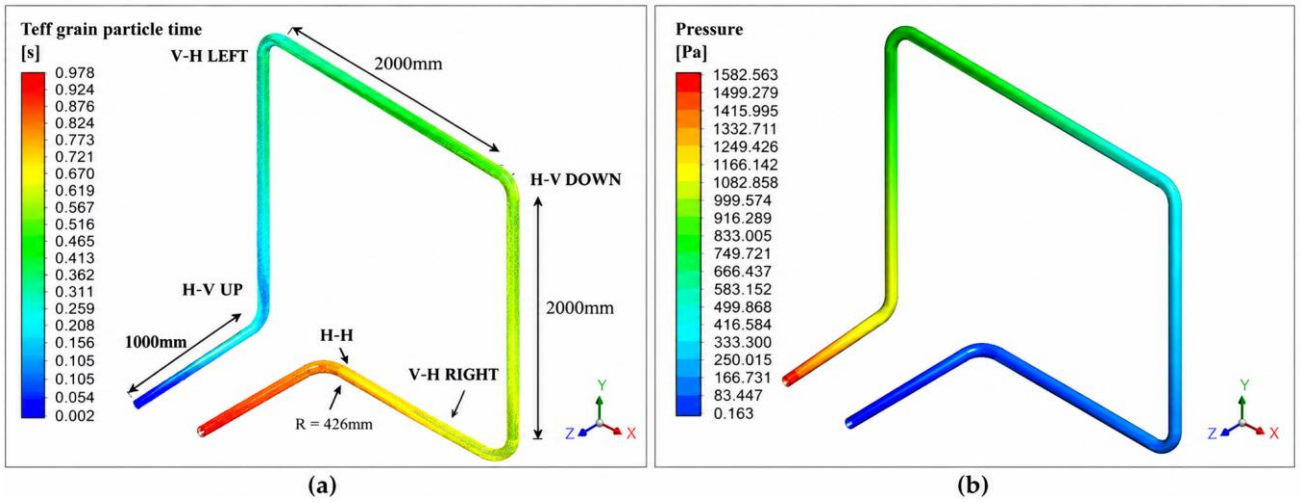


Figure 5. (a) Teff-particle residence-time distribution and (b) static-pressure contours for D = 71 mm, v = 22 m/s, and $\dot{m}_s$ = 0.13 kg/s

3.2 Local pressure fields and particle-wall interactions

Figure 5a shows that the predicted particle residence time varies along the conveying path, increasing from less than 0.05 s near the H-V UP inlet to approximately 0.98 s at the H-H junction. The longer residence time in downstream regions is consistent with particles requiring time to negotiate changes in direction and adjust their velocity after bend passage. Figure 5b presents the corresponding gas-phase static-pressure contours. The spatial pressure gradients around the bends show that pressure is not distributed uniformly through the geometry. Taken together, the panels illustrate how local flow redirection and particle response can contribute to the overall pressure loss. These contours are qualitative evidence of the flow field; the pressure-drop comparisons between layouts are quantified separately in Figures 7-8 and Tables 3-5.

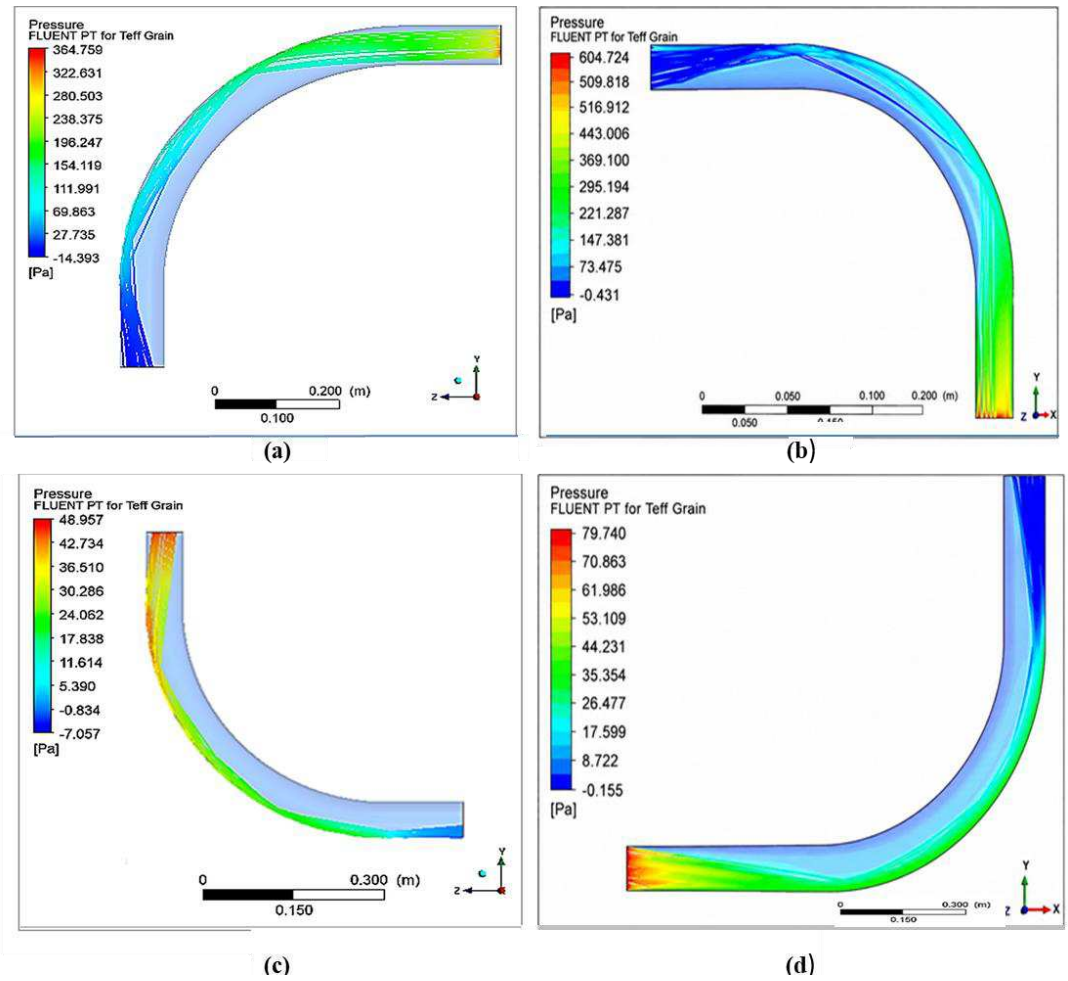


Figure 6. Local particle-phase pressure distributions for (a) the 71-mm H-V DOWN bend ($\dot{m}_s$ = 0.067 kg/s, v = 22 m/s); (b) the 46-mm V-H LEFT bend ($\dot{m}_s$ = 0.067 kg/s, v = 22 m/s); (c) the 71-mm H-H bend ($\dot{m}_s$ = 0.009 kg/s, v = 12 m/s); and (d) the 46-mm H-V UP bend ($\dot{m}_s$ = 0.009 kg/s)

3.3 Effects of pipe diameter, air velocity, and solids loading on local pressure drop

Figure 6 compares particle-phase pressure distributions for four representative cases. The panels should be read as illustrations of local pressure patterns, not as a controlled ranking of bend layouts, because pipe diameter and operating conditions differ between some panels. The higher-pressure regions near the bend and the downstream changes in pressure indicate that particle motion and gas-solid momentum exchange are spatially non-uniform. Differences between panels may reflect both the bend orientation and the different inlet conditions; therefore, the relative pressure-drop performance of the five layouts is assessed using the common operating-condition comparisons in Figures 7-8 and the statistical analyses in Tables 3-5.

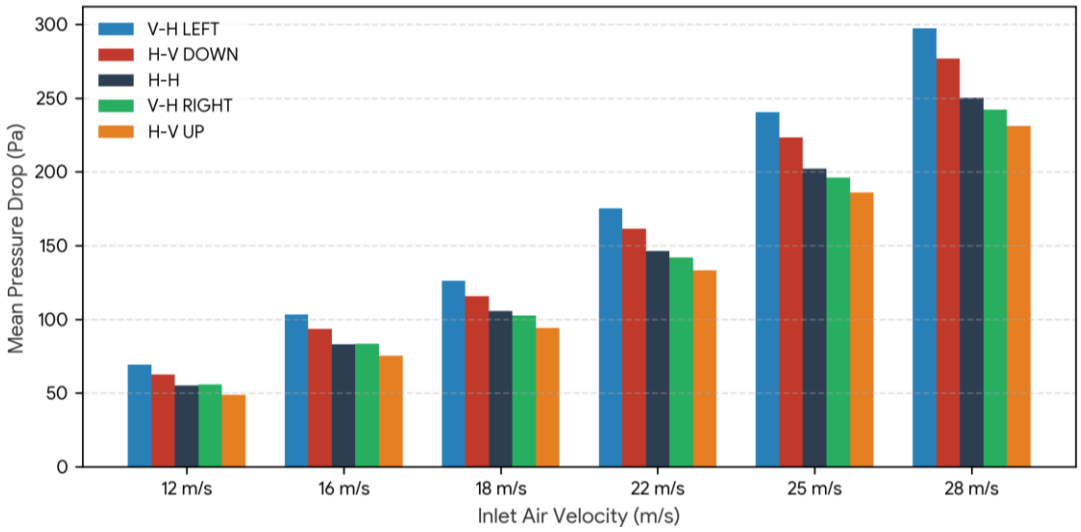


Figure 7. Mean pressure drop for the five bend layouts at the tested inlet air velocities

Figure 7 compares how the mean pressure drop changes with inlet air velocity for each layout. The layout order is the same at every velocity. The mean difference between V-H LEFT and H-V UP rises from 20.6 Pa at 12 m/s to 66.2 Pa at 28 m/s, whereas the ratio of their pressure drops falls from 1.42 to 1.29, i.e., the absolute gap grows with velocity while the relative gap narrows slightly. This pattern corresponds to the small layout × velocity interaction in Table 5.

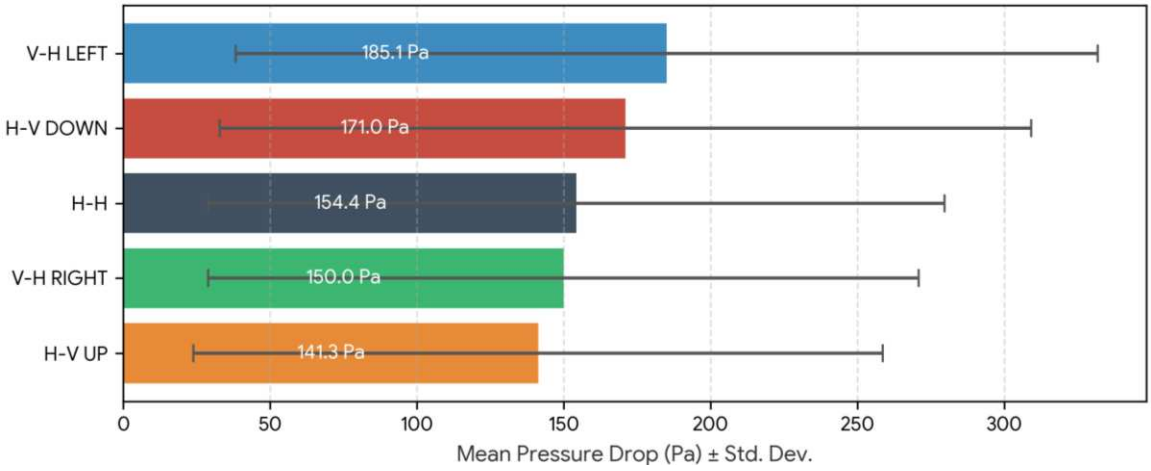


Figure 8. Overall mean pressure drop and standard deviation for each bend layout across the simulated operating conditions

Figure 8 shows the largest overall mean pressure drop for V-H LEFT (185.07 Pa) and the smallest for H-V UP (141.31 Pa). The difference is 43.76 Pa, or 23.7% of the V-H LEFT mean (V-H LEFT is 34.5% higher than H-V UP in the geometric-mean ratio, Table 4). The standard-deviation bars (about 117-147 Pa) show variation across the 144 operating conditions, which is mainly the effect of diameter, velocity and solids loading, and are not confidence intervals; layouts are compared within conditions in Section 3.4.

3.4 Statistical analysis of layout and operating-condition effects

Every layout was simulated at the same 144 operating conditions, so layouts are paired within conditions and the design is a randomised complete block with operating condition as the block (n = 144 blocks, 5 treatments, N = 720). The conditions are not a full D × v × $\dot{m}_s$ factorial (144 of 216 combinations), so the effects of D, v and $\dot{m}_s$ were estimated with Type II sums of squares from a linear model of the condition-mean ln ΔP. Pressure drop spans 25-772 Pa and the layout differences scale with ΔP, so ln ΔP was used for the interaction and condition analyses; the layout comparison is reported on the Pa scale (Tables 3 and 4) and on the log scale. Because the simulations are deterministic and each layout-condition cell has one run, the p-values express how consistently an effect appears across conditions rather than sampling error in a physical experiment, so effect sizes and confidence intervals are emphasised.

Table 3. Randomised-block ANOVA of pressure drop (Pa) for the five bend layouts with operating condition as block (N = 720)

Source of Variation	Sum of Squares (SS)	Degrees of Freedom (df)	Mean Square (MS)	F-Statistic	p-Value
Between layouts	177,252.6	4	44,313.2	291.04	< 0.001
Between operating conditions (blocks)	12,044,409.1	143	84,226.6	-	-
Residual (layout × condition)	87,091.6	572	152.3	-	-
Total	12,308,753.3	719	-	-	-

Table 3 shows a layout effect of $F(4, 572) = 291.0$, $p < 0.001$ (partial $\eta^2 = 0.67$). On the log scale $F(4, 572) = 7{,}088$. The sphericity assumption is not met (Greenhouse-Geisser $\varepsilon = 0.25$), but the corrected result is unchanged ($p < 0.001$), as is the non-parametric Friedman test ($\chi^2(4) = 575.8$, $p < 0.001$). Blocking removes the variation between operating conditions, which makes up 97.9% of the total sum of squares. The unblocked one-way ANOVA, which treats the 720 values as independent, gives only $F(4, 715) = 2.612$, $p = 0.034$ because that variation is counted as error; it is not an appropriate test for this paired design. Excluding the four rows with duplicated condition labels does not change the result ($F(4, 556) = 294.8$, $p < 0.001$).

Table 4. Pairwise comparisons of mean pressure drop between layouts (paired within the 144 conditions; Holm-adjusted p-values)

Comparison (A − B)	Mean difference (Pa)	95% CI (Pa)	Geometric mean difference (%)	Conditions with A > B (of 144)	Holm-adjusted p
V-H LEFT − H-V DOWN	14.05	12.63–15.48	+9.3	144	< 0.001
V-H LEFT − H-H	30.71	27.19–34.22	+21.5	144	< 0.001
V-H LEFT − V-H RIGHT	35.11	30.85–39.36	+24.6	144	< 0.001
V-H LEFT − H-V UP	43.75	38.91–48.59	+34.5	144	< 0.001
H-V DOWN − H-H	16.65	14.56–18.75	+11.2	144	< 0.001

H-V DOWN − V-H RIGHT	21.06	18.23–23.89	+14.0	144	< 0.001
H-V DOWN − H-V UP	29.70	26.28–33.12	+23.0	144	< 0.001
H-H − V-H RIGHT	4.40	3.67–5.14	+2.5	143	< 0.001
H-H − H-V UP	13.05	11.73–14.37	+10.7	144	< 0.001
V-H RIGHT − H-V UP	8.65	8.06–9.23	+8.0	144	< 0.001

Table 4 shows that all ten pairwise differences are significant after Holm adjustment. The ranking V-H LEFT > H-V DOWN > H-H > V-H RIGHT > H-V UP holds in 143 of the 144 conditions; in the remaining one (D = 0.120 m, v = 12 m/s, $\dot{m}_s$ = 0.009 kg/s) H-H and V-H RIGHT are equal at 30.62 Pa. The largest difference is between V-H LEFT and H-V UP (43.75 Pa, 95% CI 38.91-48.59 Pa), and the smallest between H-H and V-H RIGHT (4.40 Pa, 2.5%). Because the conditions are common to all layouts, the confidence intervals reflect how much each difference varies across conditions.

Table 5. Operating-condition effects (A, Type II, condition-mean ln ΔP, n = 144) and layout × factor interactions (B, within conditions, ln ΔP, N = 720)

Term	df	SS (ln units)	F	p-Value	Partial η^2
A: Pipe diameter (D)	2	20.912	915.92	< 0.001	0.944
A: Air velocity (v)	5	11.351	198.86	< 0.001	0.901
A: Solids mass flow ($\dot{m}_s$)	11	23.307	185.61	< 0.001	0.949
A: D × v	9	0.028	0.27	0.982	0.022
A: D × $\dot{m}_s$ (linear)	2	2.794	122.37	< 0.001	0.692
A: v × $\dot{m}_s$ (linear)	5	0.147	2.58	0.030	0.106
A: Residual	109	1.244	-	-	-
B: Layout × D	8	0.043	172.00	< 0.001	0.718
B: Layout × v	20	0.043	68.65	< 0.001	0.718
B: Layout × $\dot{m}_s$ (linear)	4	0.048	378.95	< 0.001	0.737
B: Residual	540	0.0170	-	-	-

Table 5 (part A) shows that, once layout is averaged out, pipe diameter, air velocity and solids mass-flow rate each have large effects on ΔP (partial η^2 = 0.94, 0.90 and 0.95; model R^2 = 0.981), and the D × v interaction is negligible (p = 0.98). The D × $\dot{m}_s$ interaction is large (partial η^2 = 0.69) because the solids mass-flow range differs by diameter; the interpretation of $\dot{m}_s$ is limited by the incomplete design. Part B shows that layout interacts significantly with diameter, velocity and solids mass-flow rate (all p < 0.001), but these interactions are small: together they amount to 1.7% of the layout sum of squares on the log scale (7.777), and the residual variation is small (about 1.7% of ΔP) because ΔP varies smoothly and almost proportionally between layouts. Relative to H-H, the layout ratios shift only slightly with velocity (V-H LEFT 1.26 at 12 m/s and 1.20 at 28 m/s; H-V UP 0.87 and 0.92), so the layout effect is essentially a constant proportional factor.

4. Conclusions

The pressure drop (ΔP) in five 90° bend layouts H-H, H-V DOWN, V-H LEFT, V-H RIGHT, and H-V UP was evaluated using CFD-DPM simulations across 720 total cases, comprising the same 144 operating conditions for each configuration. Model validation confirmed high accuracy against published experimental pressure drops,

yielding a mean absolute relative error of 3.40% for single-phase flow, 4.65% for gas-solid flow, and a maximum error of 5.21%. This high level of predictive fidelity strongly supports using the numerical model to evaluate and compare the layout configurations, where a clear performance ranking held across 143 of the 144 operating conditions, with only one tie.

The layout evaluation established a consistent performance ranking: V-H LEFT > H-V DOWN > H-H > V-H RIGHT > H-V UP. Statistical analysis confirmed that all ten pairwise layout differences were significant in a randomized-block analysis ($F(4, 572) = 291.0$, $p < 0.001$; Holm-adjusted pairwise $p < 0.001$). V-H LEFT produced the highest overall mean static pressure drop at 185.07 Pa, whereas H-V UP produced the lowest at 141.31 Pa. The mean difference between these extreme layouts is 43.75 Pa (95% CI: 38.91–48.59 Pa), which represents a 23.7% reduction relative to the V-H LEFT configuration. Crucially, this reflects a difference in static pressure drop across the bend section rather than a direct measurement of overall system energy savings.

Operating conditions exert the primary control over the absolute magnitude of ΔP, which ranged widely from 25 Pa to 772 Pa depending on the specific combination of pipe diameter, air velocity, and solids mass-flow rate. The geometric layouts act as an almost constant multiplier relative to the horizontal baseline layout (H-H), scaling values by approximately 1.22 for V-H LEFT, 1.11 for H-V DOWN, 0.98 for V-H RIGHT, and 0.90 for H-V UP. Although statistical interactions between layout and pipe diameter, air velocity, and mass-flow rate were detectable, they collectively account for less than 2% of the overall layout effect.

Air velocity specifically influences the scale of these pressure differences across the layouts. As air velocity increases from 12 m/s to 28 m/s, the absolute gap between the highest-drop (V-H LEFT) and lowest-drop (H-V UP) layouts widens significantly from 20.6 Pa to 66.2 Pa. Conversely, the relative performance ratio between these two extremes narrows slightly from 1.42 down to 1.29 over the same velocity range.

Author Contributions

Lemi Demissie Boset: Conceptualization, investigation, data analysis, writing original draft preparation, and writing review and editing.

Data Availability

The complete set of 720 simulated pressure-drop values (144 operating conditions × 5 layouts) is given in Supplementary Table S1.

Declarations

Funding: No funds.

Ethical approval: Not applicable.

Consent to participate: Not applicable.

Consent to publish: Not applicable.

Clinical trial number: Not applicable.

Competing interests: No competing interests.

References

[1] Boset, L. D. (2025). Determination of pressure drop in positive dilute phase pneumatic teff grain conveyor using experimental CFD-DPM simulation and ANN modeling approach. International Journal of Fluid Power, 26(1), 1-24.

[2] Kuang, S. B., Li, K. J., & Yu, A. B. (2020). CFD-DEM simulation of gas-solid flow in pneumatic conveying pipelines. Powder Technology, 367, 412-428.

[3] Senapati, M. R., & Dash, S. K. (2021). Multiphase CFD-DPM modeling of pneumatic transport in bend geometries. Journal of Fluids Engineering, 143(6), 061201.

[4] Inaba, T., & Husain, S. (2007). Experimental and numerical evaluation of pressure drop in two-phase pipe flows. International Journal of Multiphase Flow, 33(4), 389-402.

[5] Dutta, R. (2019). Numerical modeling of turbulent multiphase flows using RNG k-epsilon turbulence closure. Computers & Fluids, 185, 112-125.

[6] Dutta, R., Sharma, A., & Patel, K. (2016). Analysis of particle-wall interactions in pneumatic conveying bends using CFD-DPM. Powder Technology, 298, 77-89.

[7] Moujaes, S., & Deshmukh, A. (2018). Pressure drop characteristics across 90° pipe bends in dilute phase transport. Applied Mathematical Modelling, 62, 540-553.

[8] Klinzing, G. E., Rizk, F., Marcus, R. D., & Leung, L. S. (2010). Pneumatic Conveying of Solids: A Handbook for Engineers (3rd ed.). Springer.

[9] Marcus, R. D., Leung, L. S., Klinzing, G. E., & Rizk, F. (1990). Pneumatic Conveying Systems. Chapman and Hall.

[10] Bradley, M. S. A. (1990). Pressure drop across bends in pneumatic conveying pipelines. Powder Handling & Processing, 2(4), 311-315.

[11] McGlinchey, D. (2008). Bulk Solids Handling: Equipment Selection and Operation. Blackwell Publishing.

[12] Huber, N., & Sommerfeld, M. (1998). Modelling and numerical calculation of dilute phase pneumatic conveying in pipe systems. Powder Technology, 99(1), 90-101.

[13] Sommerfeld, M., & Lain, S. (2015). Particle motion and deposition in turbulent pipe bends. International Journal of Multiphase Flow, 71, 1-18.

[14] Zenz, F. A., & Othmer, D. F. (1960). Fluidization and Fluid-Particle Systems. Reinhold Publishing.

[15] Levy, A. (2000). Two-phase flow modeling in pneumatic conveying lines. Powder Technology, 112(1-2), 118-125.

[16] Mason, D. J., & Levy, A. (2001). Numerical simulation of particle roping in pneumatic conveying bends. Powder Technology, 119(2-3), 121-134.

[17] Yilmaz, A., & Levy, A. (2006). Particle attenuation and pressure drop in pneumatic elbows. Journal of Fluids Engineering, 128(2), 271-282.

[18] Chen, X. L., & Pereira, J. C. (2000). Computation of gas-solid two-phase flow in curved ducts. International Journal for Numerical Methods in Fluids, 33(3), 361-381.

[19] Zhang, Y., & Li, C. (2011). Numerical prediction of pressure drop in horizontal-to-vertical pneumatic conveying bends. Chemical Engineering Science, 66(14), 3210-3220.

[20] Wang, F. Y., & Shirley, S. (2014). Particle impact and wall erosion dynamics in gas-solid pipe flow. Wear, 318(1-2), 101-110.

[21] Solnordal, G. B., & Frank, M. (2015). Simulation of multiphase pressure losses in industrial elbow configurations. Industrial & Engineering Chemistry Research, 54(12), 3201-3212.

[22] Tsuji, Y., Kawaguchi, T., & Tanaka, T. (1993). Discrete particle simulation of gas-solid flows in pneumatic lines. Powder Technology, 77(1), 79-87.

[23] Bilirgen, H., & Levy, E. K. (2001). Mixing and dispersion of pulverized coal in pipe bends. Fuel Processing Technology, 71(1-3), 131-142.

[24] Kuan, B., Yang, W., & Schwarz, M. P. (2007). Dilute phase pneumatic conveying of granular materials around elbows. Chemical Engineering Science, 62(7), 1982-1996.

[25] Rose, H. E., & Duckworth, R. A. (1969). Transport of solid particles in liquids and gases. The Engineer, 227, 392-396.

[26] Chambers, A. J., & Marcus, R. D. (1986). Design of pneumatic conveying bends to minimize pressure drop and erosion. Bulk Solids Handling, 6(1), 121-129.

[27] Westman, M. A., & Michael, S. (2012). CFD analysis of gas-solid two-phase flow through 90 degree elbows. Journal of Applied Fluid Mechanics, 5(2), 45-53.

[28] Turton, R., & Levenspiel, O. (1986). A short engineering correlation to predict the terminal velocity of spheres. Powder Technology, 47(1), 83-86.

[29] Haider, A., & Levenspiel, O. (1989). Drag coefficient and terminal velocity of spherical and non-spherical particles. Powder Technology, 58(1), 63-70.

[30] Clift, R., Grace, J. R., & Weber, M. E. (1978). Bubbles, Drops, and Particles. Academic Press.

[31] Geldart, D. (1973). Types of gas fluidization. Powder Technology, 7(5), 285-292.

[32] Launder, B. E., & Spalding, D. B. (1974). The numerical computation of turbulent flows. Computer Methods in Applied Mechanics and Engineering, 3(2), 269-289.

[33] Yakhot, V., & Orszag, S. A. (1986). Renormalization group analysis of turbulence: I. Basic theory. Journal of Scientific Computing, 1(1), 3-51.

[34] Shih, T. H., Liou, W. W., Shabbir, A., Yang, Z., & Zhu, J. (1995). A new k-epsilon eddy viscosity model for high Reynolds number turbulent flows. Computers & Fluids, 24(3), 227-238.

[35] Patankar, S. V. (1980). Numerical Heat Transfer and Fluid Flow. McGraw-Hill.

[36] Rhodes, M. (2008). Introduction to Particle Technology (2nd ed.). John Wiley & Sons.

[37] Williams, A., & Agarwal, P. (2017). Parametric sensitivity analysis of gas-solid flow parameters in pipe bends. Particuology, 32, 110-121.

[38] Fokeer, S., Lowndes, I. S., & Hargreaves, D. M. (2012). Numerical simulation of coarse particle conveying in curved ducts. International Journal of Mining, Reclamation and Environment, 26(3), 205-224.

[39] Ebrahimi, M., & Schiller, L. (2013). Eulerian-Lagrangian simulations of dilute particle transport in pneumatic conveying pipes. Flow, Turbulence and Combustion, 91(4), 841-862.

[40] Akilli, H., Levy, E. K., & Sahin, B. (2001). Gas-solid flow behavior downstream of a horizontal 90° bend. Powder Technology, 116(1), 43-52.

[41] Behera, N., Agarwal, V. K., & Jones, M. G. (2013). Numerical simulation of pneumatic conveying of fine powder through a 90° bend. Particulate Science and Technology, 31(5), 485-492.

[42] Li, H., & Tomita, Y. (2000). Particle velocity and concentration distribution in horizontal pneumatic conveying bends. Powder Technology, 107(1-2), 144-152.

[43] Burnett, A. J., & Pittman, A. N. (2005). The influence of bend geometry on pressure losses in pneumatic transport lines. Journal of Pipelines, 29(2), 101-114.

[44] Pan, R. (1999). Scaling laws and pressure drop predictions for pneumatic conveying systems. Powder Handling & Processing, 11(2), 185-192.

[45] Wypych, P. W., & Arnold, P. C. (1987). On-line prediction of pressure drop in dilute and dense phase pneumatic conveying. Powder Technology, 50(3), 281-294.

[46] Sun, Z., Chen, L., Ma, G., Ma, H., & Gao, K. (2023). An experimental study on the elbow pressure drop and conveying stability of pneumatic conveying for stiff shotcrete based on response surface methodology. Processes, 11(5), 1574.

[47] Yuan, G., Liang, C., Chen, X., Xu, P., Xu, G., & Shen, L. (2014). Experimental study on pressure drop of bends in dense phase pneumatic conveying under high pressure. AIP Conference Proceedings, 1592(1), 347-357.

Supplementary Files

This is a list of supplementary files associated with this preprint. Click to download.

- SupplementaryTableS1.docx